Evaluating the Thickness of a Cyclopentane Hydrate Film Over a Sessile Water Drop Using PLIF and PIV

Muhammad A. Kamel[1], Aleksei S. Lobasov[1], Konstantin S. Pervunin[1] and Christos N. Markides[1,*]

1: Clean Energy Processes (CEP) Laboratory, Department of Chemical Engineering, Imperial College London, SW7 2AZ London, United Kingdom
* Correspondent author: c.markides@imperial.ac.uk

Keywords: Cyclopentane hydrates; Liquid-liquid interface; Water drop; Temperature difference; Heat transfer; PLIF; PIV

ABSTRACT

The accumulation of hydrates presents an important flow-assurance challenge. Herein, we performed an experimental study to quantify the thickness of a hydrate layer growing laterally along the interface of a water drop submerged in the bulk phase of cyclopentane at sub-zero temperatures. Spatially-resolved velocity and temperature measurements in both liquid phases were taken independently using particle image velocimetry, one- or two-colour planar laser-induced fluorescence. We found that the appearance of hydrates leads to a displacement of the temperature maximum away from the phase boundary, which is typically observed very close to the interface due to the recirculating motion of water inside the drop. Making an assumption that, when hydrates are absent, this recirculating motion is retained in time and the maximum position is, thus, unchanged, we conclude that this shift should indicate the hydrate layer should mostly protrude into the drop, and its thickness was evaluated to be around 0.38 ± 0.1 mm.

1. Introduction

Clathrate hydrates are inclusion compounds created by relatively small molecules of a guest medium (e.g., carbon dioxide, methane, ethane, tetrahydrofuran), which is also called as hydrate former, in the presence of water. At favourable conditions (usually low temperatures and high pressures), water molecules become oriented in such a way to form a network of cavities where molecules of a guest agent are trapped in, thus making solid crystals. The most abundant example of these crystalline structures in nature is methane hydrates (Chou et al., 2000), which are found in natural gas and crude oil reservoirs, as well as in the permafrost (Dawe & Thomas, 2007). In the oil and gas industry, pipelines are susceptible to hydrate formation, where these solids tend to accumulate, which in turn can result in obstruction of the flow causing pipe blockage and, thus, poses a significant flow-assurance challenge. Hydrates also find application in various technological processes and industrial areas, such as desalination (He et al., 2018), gas separation (Zhang et al., 2021), carbon capture and sequestration (Lee et al., 2016) and energy storage (Yu et al., 2021).

Naturally occurring hydrates require moderately high pressures, for example, upwards of 30 bar at temperatures above 0 °C for methane molecules to form a stable structure within the water cavities (Sloan & Koh, 2007). Synthesis of methane hydrates in laboratory environment requires operations with highly flammable gas compounds at elevated pressure, which poses a safety risk. Thus, there is motivation to use alternative hydrate formers in experimental studies of clathrates. For laboratory-scale research of these solid compounds, cyclopentane (or c-pentane) is a good substitute for methane as c-pentane hydrates are stable at ambient pressure and temperatures below 7 °C (Sloan & Koh, 2007). Nakajima et al. (2008) and Stoner et al. (2021) successfully verified the applicability of cyclopentane as a guest material at temperatures between 0 and 7 °C in different experimental configurations. Within this temperature range, the subcooling temperature investigated is limited to a maximum of some 7 °C, which is considerably lower than for methane hydrates with the utmost degree of subcooling of up to 22 °C (Davies et al., 2010). The reason for such a constraint on cyclopentane hydrates is mainly to avoid ice contamination during the solidification process. In our recent article (Kamel et al., 2023), we extended the low end of the working temperature range for c-pentane hydrates to as low as –7 °C, with the maximum subcooling temperature reached approximately 15 °C, demonstrating variations in the hydrate film morphology with the degree of subcooling. As cyclopentane is poorly soluble in water, hydrate crystals grow directly on their phase boundary. This process is expected to be accompanied by latent heat release at the moving front of the expanding hydrate layer due to the exothermic nature of hydrate formation.

In several studies (e.g., Freer et al., 2001; Liu et al., 2018), it was supposed that the lateral growth of hydrates is governed by heat transfer. That is why local temperature information is of high importance when investigating the spreading of a hydrate film along the interface. Due to the dynamic nature of the hydrate front, pointwise temperature measurements with a thermocouple(s) are quite challenging and intrusive to the actual hydrate formation process. Advanced laser-based measurement techniques, such as Planar Laser Induced Fluorescence (PLIF) and Particle Image Velocimetry (PIV), enable whole-field quantitative visualisation of flow temperature and velocity. Both PLIF and PIV have the advantage of being non-invasive and providing high spatial and temporal resolution, which allows for examination of the dynamics of the hydrate layer front. Both methods have been used before to study other types of phase transitions, including boiling (Voulgaropoulos et al., 2022), evaporation (Strizhak et al., 2018), freezing (Voulgaropoulos et al., 2021) and melting (Volkov & Strizhak, 2022).

In this study, we employ planar laser-induced fluorescence (PLIF) to collect instantaneous whole-field temperature data, which is beneficial in capturing the dynamics of hydrate growth, on either side of the interface of a sessile water drop submerged in cyclopentane. Temperature changes are

captured using one-colour PLIF (1c-PLIF) in the bulk phase and two-colour PLIF (2c-PLIF) inside the drop during hydrate formation. In addition, local information on variations in the instantaneous velocity pattern is extracted by particle image velocimetry (PIV). The aim of this paper is to elucidate the role of interfacial heat transfer in lateral growth of hydrates and to evaluate the thickness of the newly-formed hydrate film.

2. Experimental methods: apparatus and test conditions

The experiments were conducted in a stainless-steel hydrate cell with quartz windows on all four sides to allow optical access from different directions. The cuvette was filled with 120 mL of liquid cyclopentane with a certified purity of greater than 98% (Merck KGaA). 0.25 mL of deionised water with electrical conductivity of 10 µS/cm was then injected at a volumetric rate of 1.33×10^{-5} L/s using a Braintree Scientific BS-8000 syringe pump (6 µL/h to 1200 mL/h, 35 lbs. at minimum speed, 15 lbs. at maximum speed, accuracy = ± 0.01 mL) to create a sessile drop on a sapphire-glass substrate lying on a pedestal at the centre of the cell bottom as shown in Fig. 1a.

A standard rubber O-ring was adhered to the substrate to hold the drop with a diameter of 4.5 mm and height of 2.8 mm in place. Cooling of the system was implemented by circulating a mixture of ethylene glycol and water in a 1:1 volume ratio through the outer circuit of the cell that was connected to a Stuart SRC5 cooler (450 W, 9 L/min) for heat removal (Fig. 1a). In order to minimise heat gain from the environment, the cuvette was all-round covered with an insulation material tightly attached to its walls by an external transparent acrylic casing enveloping the cell. Condensation of moisture from ambient air on the observation windows was prevented by dehumidifying air inside the adjacent chambers (the inner space between each window and the casing) with beads of silica gel (Fig. 1a). Further, a weak stream of dry compressed air was directed from the outside onto the casing, specifically onto the areas in front of the windows, to produce a gas blanket alongside its walls to further reduce any optical distortions due to condensation in the field of view of a camera. The bulk temperature of cyclopentane was set to T_b = –3.5 °C in the experiment, which corresponded to the subcooling temperature ΔT_{sub} = 11.2 °C. More information about the experimental facility and test conditions can be found in Kamel et al. (2023).

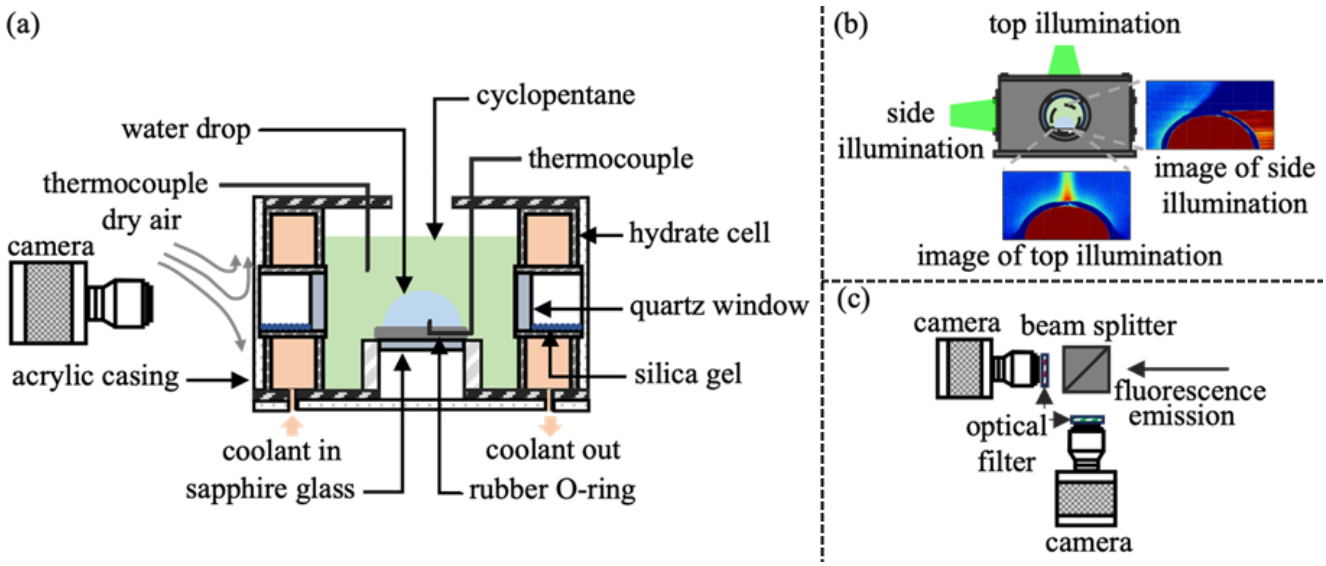

Figure. 1 Schematics of (a) the hydrate cell with indication of its main components and relative placement of the camera employed for either PLIF or PIV measurements, (b) the arrangement of the two laser sheets in the 1c-PLIF method relative to the hydrate cell together with the examples of raw images recorded by the camera with the top and side laser illumination, and (c) the optical configuration used for 2c-PLIF measurements.

3. Measurement techniques

Temperature measurements in the bulk of c-pentane and inside the water drop were taken separately using planar laser-induced fluorescence (PLIF), using one-colour (1c-PLIF) and two-colour (2c-PLIF), to detect thermal variations in both phases near the interface during lateral hydrate growth. For this, temperature-sensitive fluorescent dyes were premixed to both working liquids: Nile Red at a concentration of 1.7×10^{-6} mol/L was dissolved in cyclopentane, while Sulforhodamine B (9.6×10^{-7} mol/L) and Fluorescein 27 (1.1×10^{-5} mol/L) were added to water.

The region of interest (around or inside the drop) was illuminated by one or two double-cavity Litron pulsed Nd:YAG lasers (wavelength = 532 nm, maximum pulse energy = 200 mJ @ 15 Hz) equipped with LaVision and Dantec Dynamics sheet optics (divergence angles = 4° and 13.8°, respectively), each of which generated a thin light sheet (thickness ≈ 0.4 mm). As shown in Fig. 1b, the use of two laser sheets directed from the side and top of the cuvette was necessary particularly for 1c-PLIF measurements in the bulk phase to obtain temperature distributions over at least one half of the drop interface from its base to the apex. In this instance, both lasers were operated together in single-pulse mode, with a time delay between their pulses made as short as 55.31 μs to allow the quasi-simultaneous recording of two instantaneous fluorescence intensity fields by the

same camera running in double-frame mode. For the 2c-PLIF measurements inside the drop, a single laser operated in single-pulse mode was sufficient to illuminate the drop from beneath.

The fluorescence signals were recorded by one (1c-PLIF) or two (2c-PLIF) LaVision Imager MX 2M-160 double-frame sCMOS cameras (image resolution = 1936 × 1216 pixels, pixel pitch = 3.45 μm, digit capacity = 12 bits, maximum frame rate = 155 Hz @ 8 bits), each equipped with a Sigma 105 mm f/2.8 EX DG Macro lens. Depending on the specific configuration of the PLIF method (1c-PLIF or 2c-PLIF) and the type of the liquid where the measurements were taken (cyclopentane or water), an appropriate combination of short-pass, long-pass or notch filters was utilised. As noted above, in the case of 1c-PLIF, one camera operated in double-frame mode was only employed, whereas the application of the 2c-PLIF technique required the use of both cameras which observed the droplet through a beam splitter and captured simultaneously different fluorescence emissions characteristic of the two fluorophores (Fig. 1c). The resulting spatial resolution of 1c- and 2c-PLIF images was 49.8 and 78.6 pixel/mm, respectively, while the optical magnification of the PLIF measurement system in the according configurations was 0.17 and 0.27. The recording rate was intentionally reduced to 2 Hz to minimise the quantity of light energy absorbed by the substrate, so the heating effect due to the laser radiation can be neglected.

Velocity measurements in both phases were conducted by particle image velocimetry (PIV) independently of each other and the PLIF thermography, which required seeding of the working liquids with tracer particles. They were selected taking into account the following aspects. First, their density should be as close to that of water or c-pentane as possible to ensure their nearly neutral buoyancy so that they neither precipitate nor float. Second, their average linear size in the image should be around the optimal value (3-4 pixels) to allow accurate calculation of the iterative cross-correlation function at the stage of PIV image processing. Finally, the Stokes number must not exceed 10^{-3} for the seeding particles to neatly follow the flow streamlines. Hence, the best options were silver-coated hollow glass microspheres for cyclopentane (relative density $\rho_\mathrm{p}/\rho_\mathrm{l} = 0.98$, mean diameter $d_\mathrm{p} = 32$ μm) and fluorescent polystyrene microparticles for water ($\rho_\mathrm{p}/\rho_\mathrm{l} = 1.05$, $d_\mathrm{p} = 7.6$ μm), with their Stokes numbers being lower than 10^{-6}. The PIV measurement system was composed of the same components that were used in the PLIF thermometry, namely one Litron Nd:YAG laser (wavelength = 532 nm, maximum pulse energy = 50 mJ @ 100 Hz) with a sheet optics and one LaVision Imager MX 2M-160 camera operated in double-frame mode with a Sigma 105 mm f/2.8 EX DG Macro lens. The time delay between the frames in an image pair was 13 μs. The spatial resolution and optical magnification in the case of PIV measurements were 200 pixel/mm and 0.69, respectively. The recording rate of the PIV system was set to the same value as in the PLIF thermography for the same reason.

In order to correct for all possible optical distortions, to scale the recorded images and to compensate for angular misalignment and mismatching of optical paths of the cameras, spatial calibration of the PIV and PLIF measurement systems was performed by finding third-order polynomial transforms for each camera. This was fulfilled in the DaVis 10 software by analysing and processing corresponding photographs of a flat LaVision micro-calibration target placed in the hydrate cell such that its working surface was within the laser sheet. Almost in the entire measurement domain, the mismatch between the actual marker positions on the target and their coordinates in its virtually reconstructed model was smaller than 1 pixel.

4. Data Processing

4.1 Fluorescence

Each ensemble of PLIF images corresponding to a certain experimental run was processed using the following procedures one after another. The parasitic background signal resulting from the dark current and thermal noise of the camera matrix, multiple reflections of the laser irradiation and background Illumination from other light sources, was evaluated by taking the average of a set of at least 200 background images that were recorded when the lasers were in operation, with no fluorophore added to the liquids. The average background intensity field with a maximum brightness of 40 counts out of 4096 in total was then subtracted from each instantaneous PLIF image in the ensemble. In the case of 1c-PLIF measurements in cyclopentane, the effects of spatial nonuniformity of intensity distribution across the laser light sheet and progressive extinction of this exciting radiation along the path of its propagation due to its absorption by the stain were taken into account by capturing at least 100 test images prior to each experimental run (i.e., without the drop injected) after stabilisation of the bulk temperature at the pre-set level. Pulse-to-pulse variations of the laser radiation energy in the experiment were cancelled by adjusting the overall fluorescence intensity in an instantaneous field to a reference value. For this, the instantaneous fluorescence signal, which is considered to be only dependent of and directly proportional to the local density of the laser radiation energy, was spatiotemporally averaged over a 20×20-pixel region, sufficiently distant from the water drop (the upper left corner of the intensity field in this study) to be unsusceptible to reflections from the interface, and across the entire ensemble of PLIF images, thus providing the reference value. For 2c-PLIF measurements, to minimise the influences of nonuniformity of radiation energy distribution within the laser sheet, excitation light extinction and overlapping of the emission and absorption fluorescence spectra

(self-absorption) of both stains, the resulting PLIF images from each camera were individually multiplied with corresponding flat-field patterns. The latter contained a uniform temperature distribution across the field of view of each camera and were beforehand recorded in the water drop at least 5 min after stabilisation of the bulk temperature of cyclopentane.

Temperature calibration of 1c-PLIF, where Nile Red was dissolved in cyclopentane, and 2c-PLIF, with Fluorescein-27 and Sulforhadamine B added to water, was performed using reference data on temperature measured independently. For this, a 0.5-mm T-type TC Direct thermocouple (response time = 0.03 s, measurement uncertainty = ± 0.1 °C) was inserted in cyclopentane from above or in water from under the rubber O-ring at the drop base to be close to the measurement plane but not to obstruct the laser sheet to avoid undesired reflections, which could introduce additional error to the PLIF measurement. The data acquisition rate of the thermocouple was set to 1 Hz. The calibration procedure was started at least 5 min after stabilisation of the bulk temperature of cyclopentane or water in the drop. PLIF images and temperature data from the thermocouple were recorded together for the bulk temperature varied from –8 to 16 °C in c-pentane and from –7 to 16 °C in water. At each temperature level, 200 PLIF images were captured by each camera, processed using the same routine as previously described and spatiotemporally averaged over a 0.5 × 0.5-mm image area next to the thermocouple tip and across the entire ensemble. These datapoints were then used to fit a temperature calibration curve as shown in Fig. 2. The temperature sensitivity in the experiment was 1.9 %/°C (1c-PLIF) and 2.9 %/°C (2c-PLIF), while the measurement uncertainty was ± 0.3 °C and ± 0.4 °C, respectively.

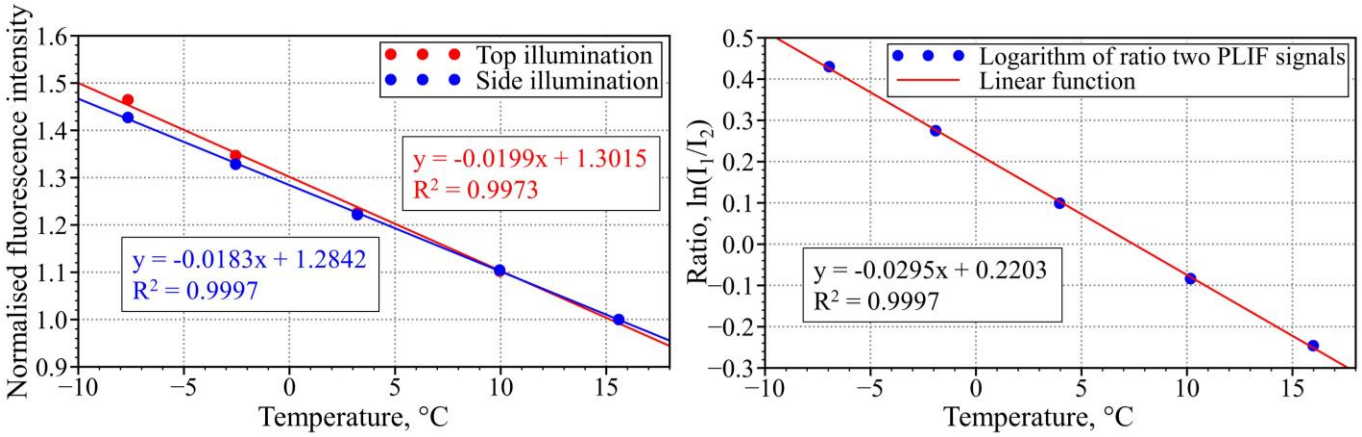

Figure. 2 (a) The fluorescence intensity of Nile Red in cyclopentane as a function of temperature for the top and side illumination, and (b) calibration curve of the intensity ratio of the two fluorescent dyes (Sulforhodamine B and Fluorescein-27) in water against temperature.

4.2 Velocimetry

PIV images were processed in the DaVis software. First, they were overlaid with a geometric mask to remove areas outside of the region of interest. While processing each ensemble of PIV images, the shape of this mask was modified stepwise using a Python code because the position of the drop interface changed during the cooling process, thus ensuring adequate capture of the velocity near the interface. Then the 'subtract sliding background' procedure with a 4-pixel filter length was implemented to enhance the intensity difference between the tracers and background in the images to aid particle identification at the following step. For evaluation of the local displacement of the seeds, an iterative cross-correlation algorithm with continuous shift and deformation of the interrogation windows was used. The initial size of the computational cells was set to 256 × 256 pixels, which was reduced to the final size of 64 × 64 pixels after four iterations. The spatial overlapping between the interrogation windows was equal to 50%. In order to improve the accuracy of velocity evaluation, we utilised the so-called multipass approach of vector calculation, where a sliding sum of the correlation coefficient is computed based on information for several consecutive measurements, including the current one, to ensure the same tracers are correlated with each other. The spatial resolution of the velocity fields was approximately 0.32 mm/vector with a grid spacing of 0.16 mm. The measurement uncertainty of the PIV method was estimated to be 2% to 4% depending on the particle displacement.

5. Results and Discussion

Figure 3 shows the combined images of the three independent datasets (1c-PLIF, 2c-PLIF and PIV) in both phases for the cases when: (i) hydrates are absent (Fig. 3a), and (ii) they eventually appear (Fig. 3b). In order to discover the effect of hydrates on the temperature distributions in both instances, we compare the combined fields at two characteristic moments: $t = 10$ and 180 s, where $t = 0$ s corresponds to the point of time when the syringe needle used to inject water was pulled out of the hydrate cell after creating of the drop. As 25 mL of water at room temperature was introduced into the bulk cyclopentane phase being at $T_b = -3.5$ °C, the newly established drop experienced quick cooling due to heat transfer to the surrounding liquid. This is clearly visible in Fig. 3a-i and 3b-i by a warm region over the top half of the drop, leading to a strong temperature gradient in cyclopentane between the interface and the bulk. The maximum temperature was achieved in a region over the very apex in both cases.

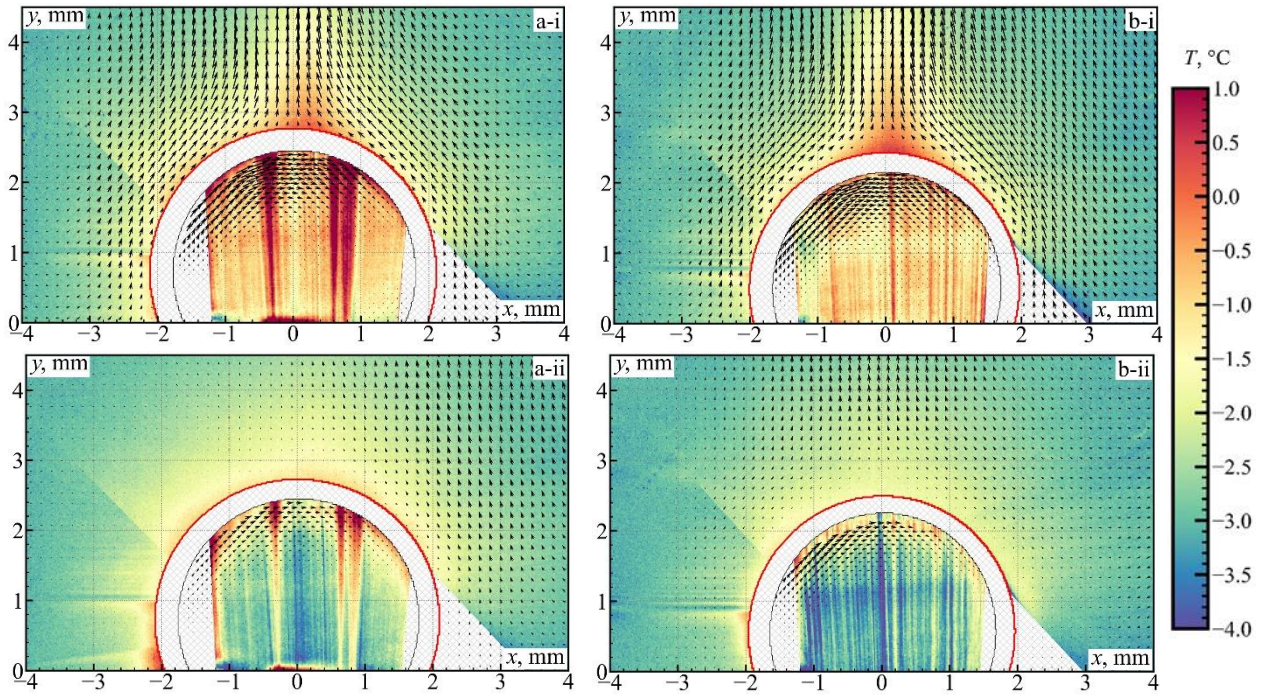

Figure. 3 Combined temperature (colour maps) and velocity (vector fields) distributions measured independently in both phases for two cases: (a) in the absence, and (b) in the presence of hydrates, at two characteristic instances: (i) t = 10 s (i.e., during intensive drop cooling), and (ii) after 180 s lapsed from the drop injection. As the velocity magnitude in water is on average much smaller than that in cyclopentane, the length of the displayed vectors inside the drop is increased by 10 times to appear clear in the images. The thick red arc depicts the outer drop interface, while the black one demarcates the region inside the drop where the measurements were taken. The white areas inside and to the right of the drop display the invisible zone and shadow present in the experiment.

At the very beginning of the cooling process, the temperature difference between the drop and the surrounding cyclopentane is very high, which induces intensive natural convection inside both liquids. This explains the presence of the region of increased temperatures immediately above the drop apex (stagnation point), where cyclopentane density must be substantially reduced due to heat transfer, and a strong buoyancy effect must take place, which is additionally confirmed by the measured velocity fields (Fig. 3a-i and 3b-i). As the thermal relaxation time $t_{th} = h^2/\alpha_{\mathrm{w}}$ passed, where h is the drop height and α_{w} is the thermal diffusivity of water, which is approximately 48 s in our experiment, the water drop is expected to attain a close-to-equilibrium state around T_{b}. After this, the effect of convection should become much weaker. Figures 3a-ii and 3b-ii confirm this conjecture, revealing more uniform temperature distributions in the drop and the bulk of cyclopentane, as well as a decrease in the velocity magnitude (cf. Fig. 3a-i and 3b-i).

Figure 4 shows the profiles of local temperature T deep into both phases down to 1 mm from the interface. At $t = 10$ s, the temperature distribution in the drop appears abnormal as the maximum of T is achieved inside a very narrow layer under the interface within the invisible zone (more precisely, it should lie in the range of –0.2 mm $< r <$ 0 mm) but not deeper into the water phase (Fig. 4a). This can be explained by the strong recirculating motion taking place in the drop as a result of natural convection, carrying warm water from the depth to the apex along the interface (Fig. 3a-i and 3b-i). Cyclopentane just takes heat away from the drop (Fig. 4a). Similar distributions of T in both phases are also observed at $t = 180$ s in the case where hydrates are absent (Fig. 4b). However, if hydrates are formed, the T peak finally comes out of the invisible domain to be clearly pronounced at $r_{T=\max} = -0.48$ mm (Fig. 4b). Thus, assuming that the recirculating motion is kept, though becoming obviously weaker (Fig. 3a-ii and 3-ii), and the T maximum keeps its position with time in the case without hydrates, we can conjecture that the hydrate film should mostly protrude into water and its thickness should be at least 0.38 ± 0.1 mm.

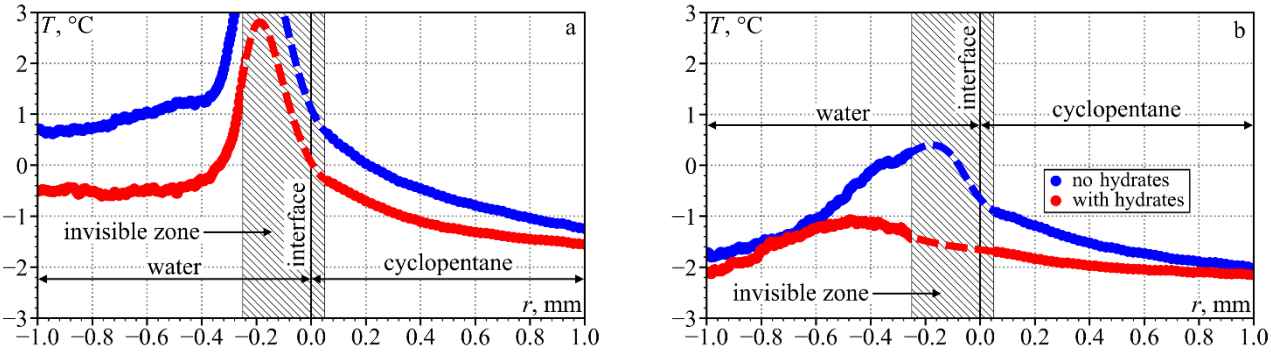

Figure. 4 Profiles of local instantaneous temperature along the perpendicular to the interface in both liquids, which were constructed near the drop apex after: (a) t = 10 s, and (b) t = 180 s from water injection. The blue and red dashed curves show expected shapes of the profiles within the invisible domain.

6. Conclusions

Using 1c-PLIF, 2c-PLIF and PIV, we measured independently instantaneous temperature and velocity fields inside a water drop and in the bulk phase of cyclopentane. Initially, water at room temperature was injected into c-pentane being at a sub-zero temperature. As a result, the drop was intensively cooled down due to heat transfer to the surrounding liquid, with a strong recirculating motion occurred inside the water phase, which is consistent with the obtained thermal map in cyclopentane. We found that the maximum of temperature was unexpectedly achieved in a very narrow layer (not exceeding 0.2 mm in thickness) inside the drop near the interface as a result of the strong recirculation of water. Over time, if hydrates are absent, the position of this peak is

highly likely kept unchanged or wiggles around insignificantly as the recirculating behaviour retains, though becoming weaker. However, the formation of hydrates leads to a displacement of this temperature peak deeper into the drop (i.e., farther from the interface) such that it is found at a distance of 0.48 mm away from the phase boundary. This shift indicates that the hydrate film should mostly protrude into the water phase, while the thickness of the hydrate layer should not be less than 0.38 ± 0.1 mm.

Acknowledgments

The research was supported by a PhD studentship from the Malaysian People's Trust Council (Majlis Amanah Rakyat, MARA). Data supporting this publication can be obtained on request from cep-lab@imperial.ac.uk. For the purpose of Open Access, the authors have applied a CC BY public copyright licence to any Author Accepted Manuscript version arising from this submission.

References

Chou, I. M., Sharma, A., Burruss, R. C., Shu, J., Mao, H. K., Hemley, R. J., ... & Kirby, S. H. (2000). Transformations in methane hydrates. *Proceedings of the National Academy of Sciences*, *97*(25), 13484-13487.

Davies, S. R., Sloan, E. D., Sum, A. K., & Koh, C. A. (2010). In situ studies of the mass transfer mechanism across a methane hydrate film using high-resolution confocal Raman spectroscopy. *The Journal of Physical Chemistry C*, *114*(2), 1173-1180.

Dawe, R. A., & Thomas, S. (2007). A large potential methane source—Natural gas hydrates. *Energy Sources, Part A*, *29*(3), 217-229.

Freer, E. M., Selim, M. S., & Sloan Jr, E. D. (2001). Methane hydrate film growth kinetics. Fluid Phase Equilibria, 185(1-2), 65-75.

He, T., Nair, S. K., Babu, P., Linga, P., & Karimi, I. A. (2018). A novel conceptual design of hydrate based desalination (HyDesal) process by utilizing LNG cold energy. *Applied energy*, 222, 13-24.

Kamel, M. A., Lobasov, A. S., Narayan, S., Pervunin, K. S., & Markides, C. N. (2023). Hydrate Growth over a Sessile Drop of Water in Cyclopentane. Crystal Growth & Design.

Lee, Y., Lee, D., Lee, J. W., & Seo, Y. (2016). Enclathration of CO2 as a co-guest of structure H hydrates and its implications for CO2 capture and sequestration. Applied Energy, 163, 51-59.

Liu, Z., Li, H., Chen, L., & Sun, B. (2018). A new model of and insight into hydrate film lateral growth along the gas–liquid interface considering natural convection heat transfer. Energy & Fuels, 32(2), 2053-2063.

Nakajima, M., Ohmura, R., & Mori, Y. H. (2008). Clathrate hydrate formation from cyclopentane-in-water emulsions. *Industrial & Engineering Chemistry Research*, *47*(22), 8933-8939.

Sloan Jr, E. D., & Koh, C. A. (2007). *Clathrate hydrates of natural gases*. CRC press.

Stoner, H. M., Phan, A., Striolo, A., & Koh, C. A. (2021). Water wettability coupled with film growth on realistic cyclopentane hydrate surfaces. Langmuir, 37(42), 12447-12456.

Strizhak, P. A., Volkov, R. S., Misyura, S. Y., Lezhnin, S. I., & Morozov, V. S. (2018). The role of convection in gas and liquid phases at droplet evaporation. International Journal of Thermal Sciences, 134, 421-439.

Volkov, R., & Strizhak, P. (2022). Temperature recording of the ice–water system using planar laser induced fluorescence. *Experimental Thermal and Fluid Science*, *131*, 110532.

Voulgaropoulos, V., Kadivar, M., Moghimi, M. A., Maher, M., Alawadi, H., Matar, O. K., & Markides, C. N. (2021). A combined experimental and computational study of phase-change dynamics and flow inside a sessile water droplet freezing due to interfacial heat transfer. International Journal of Heat and Mass Transfer, 180, 121803.

Voulgaropoulos, V., Aguiar, G. M., Markides, C. N., & Bucci, M. (2022). Simultaneous laser-induced fluorescence, particle image velocimetry and infrared thermography for the investigation of the flow and heat transfer characteristics of nucleating vapour bubbles. International Journal of Heat and Mass Transfer, 187, 122525.

Yu, Y. S., Zhang, X., Liu, J. W., Lee, Y., & Li, X. S. (2021). Natural gas hydrate resources and hydrate technologies: a review and analysis of the associated energy and global warming challenges. *Energy & Environmental Science*, *14*(11), 5611-5668.

Zhang, Q., Zheng, J., Zhang, B., & Linga, P. (2021). Coal mine gas separation of methane via clathrate hydrate process aided by tetrahydrofuran and amino acids. Applied Energy, 287, 11657